Characterization of the optic disc in retinal imagery using a probabilistic approach

Kenneth W. Tobin[*a], Edward Chaum[b], V. Priya Govindasamy[a], Thomas P. Karnowski[a], Omer Sezer[c]

[a]Oak Ridge National Laboratory[†], Oak Ridge, Tennessee
[b]University of Tennessee Health Science Center, Memphis, Tennessee
[c]University of Tennessee, Knoxville, Tennessee

ABSTRACT

The application of computer based image analysis to the diagnosis of retinal disease is rapidly becoming a reality due to the broad-based acceptance of electronic imaging devices throughout the medical community and through the collection and accumulation of large patient histories in picture archiving and communications systems. Advances in the imaging of ocular anatomy and pathology can now provide data to diagnose and quantify specific diseases such as diabetic retinopathy (DR). Visual disability and blindness have a profound socioeconomic impact upon the diabetic population and DR is the leading cause of new blindness in working-age adults in the industrialized world. To reduce the impact of diabetes on vision loss, robust automation is required to achieve productive computer-based screening of large at-risk populations at lower cost. Through this research we are developing automation methods for locating and characterizing important structures in the human retina such as the vascular arcades, optic nerve, macula, and lesions. In this paper we present results for the automatic detection of the optic nerve using digital red-free fundus photography. Our method relies on the accurate segmentation of the vasculature of the retina along with spatial probability distributions describing the luminance across the retina and the density, average thickness, and average orientation of the vasculature in relation to the position of the optic nerve. With these features and other prior knowledge, we predict the location of the optic nerve in the retina using a two-class, Bayesian classifier. We report 81% detection performance on a broad range of red-free fundus images representing a population of over 345 patients with 19 different pathologies associated with DR.

Keywords: diabetic retinopathy, red-free fundus imagery, vascular segmentation, optic nerve detection, Bayesian classifier, feature analysis

1. INTRODUCTION

The World Health Organization estimates that 135 million people have diabetes mellitus worldwide and that the number of people with diabetes will increase to 300 million by the year 2025 [1]. More than 18 million Americans currently have diabetes and the number of adults with the disease is projected to more than double by the year 2050 [2]. An additional 16 million adults between the ages of 40-74 have pre-diabetes and are at high risk for developing diabetes. Visual disability and blindness have a profound socioeconomic impact upon the diabetic population and diabetic retinopathy (DR) is the leading cause of new blindness in working-age adults in the industrialized world [2]. The prevalence rates for DR and vision-threatening DR in adults over age 40 is 40.3% and 8.2%, respectively [3]. It is estimated that as much as $167 million dollars and 71,000-85,000 sight-years could be saved annually in the U.S. alone with improved screening methods just for DR [4].

One approach to address this issue is to develop inexpensive, broad-based screening programs for DR that would have a significant impact on the economic and social consequences of vision loss from this disease. Treatment for DR is available; the challenge lies in finding a cost-effective approach with high sensitivity and specificity that can be applied to efficient, *real-time* population-based screening to identify those who are at risk in the early stages of the disease. The application of computer based image analysis has the potential to provide low-cost, widely distributed systems. Advances in the imaging of ocular anatomy and pathology can now provide the digital data required to diagnose and

[*]tobinkwjr@ornl.gov; phone 865-574-8521; fax 865-576-8380; www.ornl.gov/sci/ismv
[†]This paper was prepared by the OAK RIDGE NATIONAL LABORATORY, Oak Ridge, Tennessee, 37831-6285, operated by UT-BATTELLE, LLC for the U.S. DEPARTMENT OF ENERGY under contract DE-AC05-00OR22725.

quantify specific diseases with computer-based systems, of which DR is only a subset. What is required is robust image analysis and automation to achieve productive computer-based screening of large populations. In this paper, we describe a method for the detection of the optic nerve based on segmentation of the vascular arcades. Detection of these anatomic structures is fundamental to the subsequent characterization of the normal or disease state that may exist in the retina.

The use of digital retinal imagery to analyze DR has been reported in numerous studies (see e.g., Refs. [5, 6, 7]). Image analysis algorithms have demonstrated the ability to detect features of DR such as exudates and microaneurysms using color and monochromatic retinal images. Fig. 1 shows an example of a red-free fundus image exhibiting several examples of lesions and hemorrhages. These small pilot studies have shown that between 75% - 85% sensitivity and specificity for certain features of DR can be achieved. Other approaches to digital image analysis of the retina have included; scotoma mapping,[8] spectral imaging,[9] scanning laser ophthalmoscopy, image extraction algorithms, and artificial neural networks [10, 11]. Studies by these groups and established retinal reading centers such as the Joslin Vision Network (Boston, MA), and Inoveon Corp. (Oklahoma City, OK) have shown that digital photography is an excellent tool for identifying DR when performed by experienced, certified readers [12, 13].

Moving beyond the current requirements of a certified human reader is a requisite for achieving broad-based, high-throughput, and low-cost screening. To achieve increased levels of automation in the digital analysis of retinal disease it is required that the important structures of the eye be systematically and reliably located. Key elements of this process include the ability to normalize a large population of images to accommodate acceptable variations in illumination and contrast from fundus cameras used for data acquisition [14]. Detection and segmentation of the vascular structure [15, 16, 17] is just as critical due to the geometric relationship that exists between the vasculature and the position of the optic disk in the retina [18, 19].

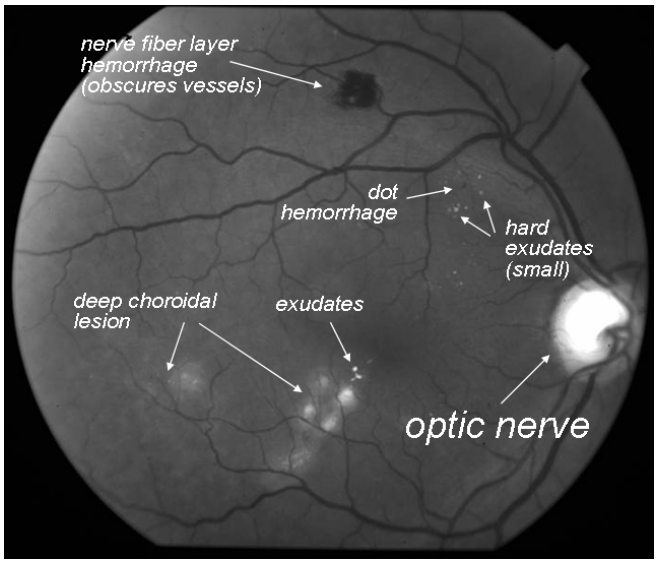

Fig. 1. Red-free fundus image showing the optic nerve, vascular arcades, and a variety of lesions.

Through this paper we contribute a novel method for localizing the optic nerve. This is a probabilistic approach using a two-class Bayesian decision rule for classifying an image pixel as *optic nerve* or *not optic nerve*. This is achieved by using statistical features of the vasculature with a multivariate normal density function [20]. This multivariate density function is derived from statistical features of the vascular structure that include the density, thickness, and orientation for every image pixel. Detection of the optic nerve represents an early step in our research to place a coordinate system on the retina that will be used to describe the relationship between retinal lesions, edema, and hemorrhages, relative to the optic disc and macula positions.

2. METHOD

The literature contains many examples of optic nerve (ON) detection in fundus imagery. These methods incorporate techniques such as dynamic contours [21], fuzzy convergence [22], and the application of geometric models [18]. In most cases, these methods rely on first segmenting the vasculature. The vasculature that feeds the retina enters the eye through the ON and branches out accordingly. Therefore, following or otherwise analyzing the structure of the vascular tree has proved to be a productive means of locating the ON. For our research we have taken a similar approach, but unlike other methods that attempt to follow the branching of the vascular tree, we have developed a method that takes advantage of a number of visual attributes of the tree in a probabilistic framework. Our goal is to accommodate a number of disease states, from mild to severe retinopathy, that result in large variations in the morphology of the visible retina. Fig. 2 presents an overview of our method. In (a) the original red-free fundus image undergoes analysis to

provide a segmentation of the vessels as shown on the top left of (b). Note also in (a) that we have a prior probability for the location of the ON that comes from training data. The prior probability shows the likely location of the center of the ON for all patients (i.e., both right and left eyes) in the training set.

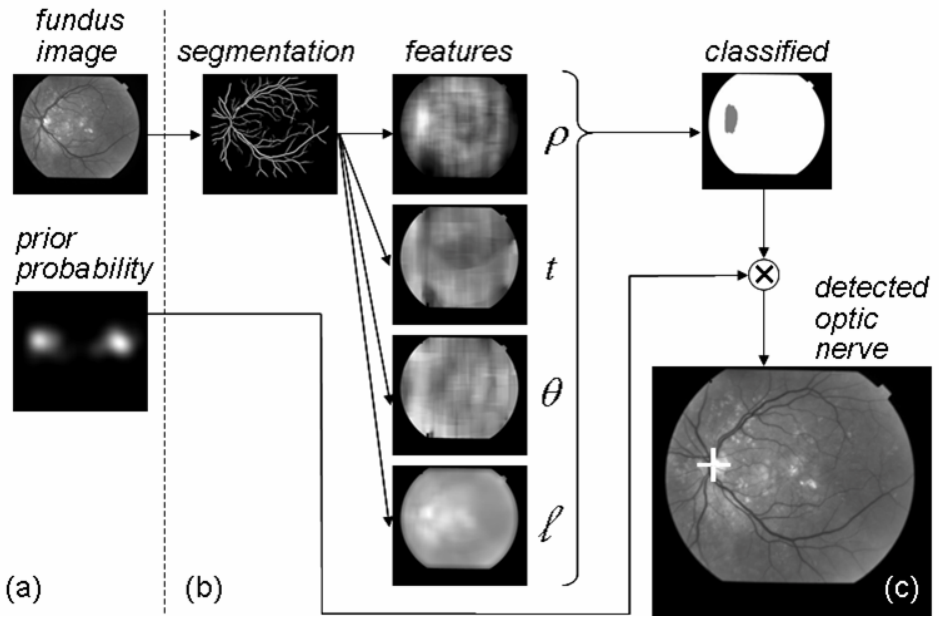

Fig. 2. Overview of optic nerve detection process. (a) Original input red-free fundus image and prior probability of optic nerve locations from training data. (b) Segmentation, feature analysis and classification process resulting in (c), detected optic nerve location in "+" position.

Since the vasculature emanates from the ON, we have opted to characterize the retina in terms of this vessel structure by defining three vessel-related features and one luminance feature. These features are a density map of the vessels, $\rho(i,j)$, an average thickness map, $t(i,j)$, an average orientation map, $\theta(i,j)$, and a luminance map $\ell(i,j)$. These features are used along with a training set of data to classify each pixel in the image as either "ON" or "not ON". Once a classification map has been obtained, the prior probabilities are combined with the classification map to determine the most likely location of the ON as shown in Fig. 2 (c). The process of segmentation, feature generation, and classification are detailed in the remainder of this section.

2.1. Segmentation of the Vasculature

We have chosen to segment the vessels in the retina using a mathematical morphology method as proposed by Zana and Klein [23]. This method was developed to detect vessel-like patterns in medical images by using a model that incorporates local linearity of the vessels, piece-wise connectivity, and vessel brightness with a Gaussian-like profile. In the paper, the method was applied to fluorescein angiography (FA) images of the retina. FA results in florescence of a sodium fluorescein dye as it courses through the vasculature, therefore developing bright images of the vessel tree. For our application with red-free fundus images, our vessel structures are dark relative to the retinal surface (see for example the vessels in Fig. 1) and the algorithm was modified accordingly.

Our goal is to produce a binary image of the vasculature, $b(i,j)$, for an image of size I×J. We want to achieve a robust segmentation for a wide variety of images representing various states of retinal disease. Fig. 3 shows three examples of vessel segmentation applied to red-free fundus images for three patients with mild age-related macular degeneration (AMD). These images (i.e., the top row) represent a variety of image textures, intensities, and long and short-term illumination variations due to patient physiology, settings on the fundus camera, and differing states of disease.

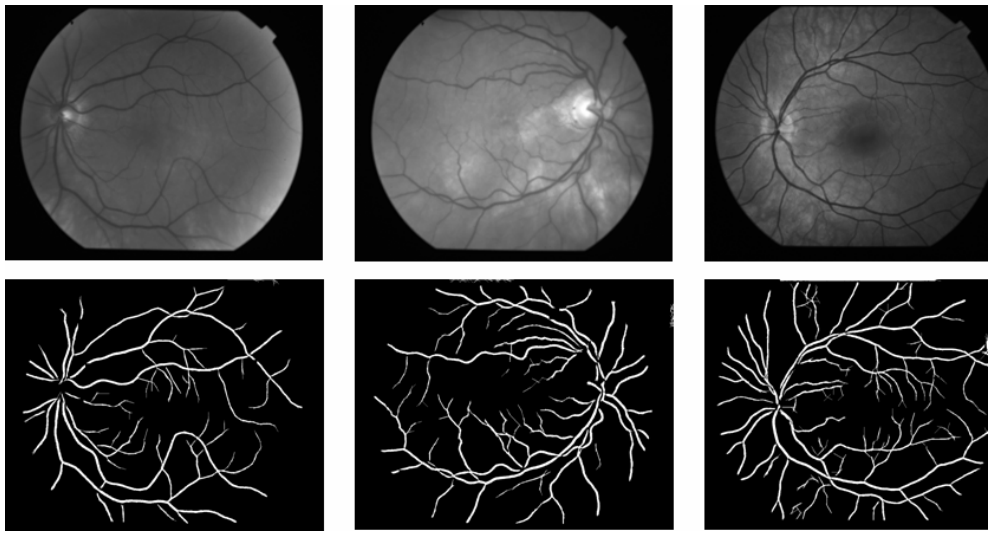

Fig. 3. The binary image results, *b(i,j)*, of a vascular segmentation for three patients with age-related macular degeneration. Notice the variation in contrast and structure from left to right; a left eye with fairly uniform reflectance with low contrast of the vessel structure, a right eye with mottled texture due to a light retinal pigmented epithelial layer, and a left eye with a high contrast vasculature and a dark macula region (center).

2.2. Feature Generation

We use the binary representation of the segmented vasculature along with a luminance representation of the retinal image to generate four descriptive features used in classifying image pixels as belonging to the ON. These features encapsulate four separate characteristics of the vessel structure that we have empirically determined are relevant to the location of the ON. These characteristics are as follows:

Retina luminance, $\ell(i,j)$ – It is characteristic of fundus imagery that the optic nerve efficiently reflects the camera illumination resulting in a brightness relative to the surrounding tissue. This is due partly to the lack of pigmentation in this area that is characteristic of the retinal pigmented epithelial layer. A feature that measures brightness can be helpful for locating the ON but can also create confusion since a myriad of retinal lesions also appear as bright objects in fundus imagery.

Vessel density, $\rho(i,j)$ – Since the vasculature that feeds the retina enters the eye through the ON, the vessels tend to be the most dense in this region; density being defined as the number of vessels existing in a unit area of the retina.

Average vessel thickness, $t(i,j)$ – Vessels are also observed to be thickest near the ON since most branching of both the arterial and venous structures does not take place until the tree is more distal from the ON.

Average vessel orientation, $\theta(i,j)$ – Finally, for the datasets that we encounter in our work, the vessels entering the eye are roughly perpendicular to the horizontal raphe of the retina. i.e., the demarcation line running through the ON and fovea. The result is an observation of vascular orientation being $\pm 90^{o}$ relative to the horizontal raphe when entering the eye and becoming more parallel (i.e., 0^{o}) as the distance from the ON increases.

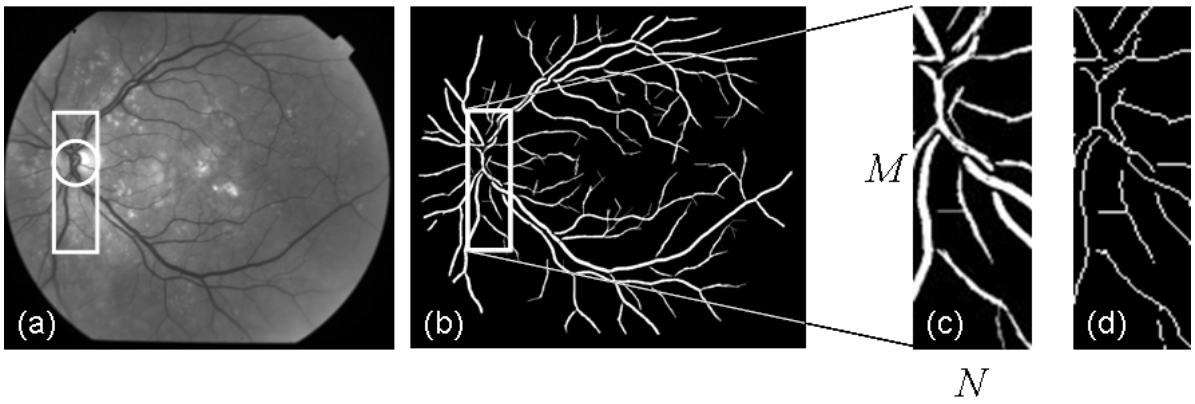

Fig. 4. Example of convolution window of size M×N in original image *I(i,j)*, roughly 3 times the diameter of the ON tall by 1 diameter wide in (a). Segmented vasculature in (b) showing filter window of size M×N for the binary image *b(i,j)* in (c) and corresponding morphologically thinned region $b_t(i,j)$ in (d).

The region of support that we have chosen to determine statistical measurements of these quantities at a point *(i,j)* in the image has been defined according to an empirical observation. Fig. 4 shows an example of a filter window of size M×N. In (a) this has been superimposed over a circular representation of the location of the ON. To measure our statistical properties of density, thickness, orientation, etc., we have chosen a rectangular convolution window that is roughly three times the diameter of the ON in height and one diameter wide. This filter window is shown superimposed on the binary segmentation of the vessel structure, *b(i,j)*, in (b) and (c). The window shown in (d) represents a morphologically thinned version of *b(i,j)*, denoted by $b_t(i,j)$. Using this terminology, the vascular density is defined as,

$$\rho(i,j)=\frac{1}{M\cdot N}\sum_{m=0}^{M-1}\sum_{n=0}^{N-1}b_t(i-m,j-n), \qquad \textbf{Eq. 1}$$

which results in a measure of the number of vessel structures in a supporting M×N region for every point *(i,j)* in the image. The average vascular thickness is defined as,

$$t(i,j)=\frac{\sum_{m=0}^{M-1}\sum_{n=0}^{N-1}b(i-m,j-n)}{\sum_{m=0}^{M-1}\sum_{n=0}^{N-1}b_t(i-m,j-n)}\ , \qquad \textbf{Eq. 2}$$

which results in a measure of the average vessel thickness in a supporting M×N region for every point *(i,j)* in the image. Note that the thickness is independent of the quantity of vessels in the support region. The luminance is determined using the same convolution window structure but it is applied to the original image, *I(i,j)*, i.e.,

$$\ell(i,j)=\frac{1}{M\cdot N}\sum_{m=0}^{M-1}\sum_{n=0}^{N-1}I(i-m,j-m)\ . \qquad \textbf{Eq. 3}$$

The average orientation is derived from the original image, *I(i,j)*, after application of a steering filter. For this research we have implemented the steering filter algorithm of Freeman and Adelson [24]. The steering filter we incorporate uses a second derivative Gaussian combined with a Hilbert transform of this derivative, i.e., $E_2(\theta) = [G_2^{\theta}]^2+[H_2^{\theta}]^2$, which can be expressed as a Fourier series in angle giving, $E_2(\theta) = C_1+C_2\cos(2\theta)+C_3\sin(2\theta)+\ldots$*[high order terms]*. The orientation image is then approximately expressed as $\theta = arg[C_2,C_3]/2$. Fig. 5 (a) shows a scaled example of the post filtered image displayed as $\cos[\theta(i,j)]$. The angles of interest in a support region, M×N, (i.e., Fig. 5 (b)) are obtained by

sampling the filtered image using the thinned binary image, $b_t(i,j)$, shown in Fig. 4 (d) resulting in a sampling as shown in Fig. 5 (c). The average orientation function is therefore expressed as,

$$\theta(i,j) = \frac{1}{M \cdot N} \sum_{m=0}^{M-1} \sum_{n=0}^{N-1} b_t(i-m, j-n) \cdot \cos\theta(i-m, j-n) \ . \qquad \textbf{Eq. 4}$$

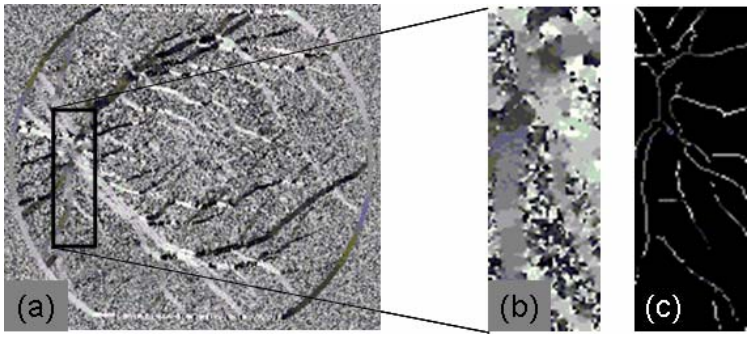

Fig. 5. (a) Example of the result of the steering filter applied to the original red-free fundus image shown in Fig. 4. (b) Filter region of size M×N and region after further filtering with the binary thinned image in (c). The final result in (c) is used to determine the average orientation of the vasculature in the region.

Fig. 6 shows examples of the vascular segmentation and the feature maps developed for four different fundus images in rows (a) through (d). Each position in the original image, *(i,j)*, now has associated with it a descriptive multivariate vector, $\boldsymbol{v}(i,j) = [\ell,\rho,\theta,t]^t$, that will be used for ON classification as described in the following section.

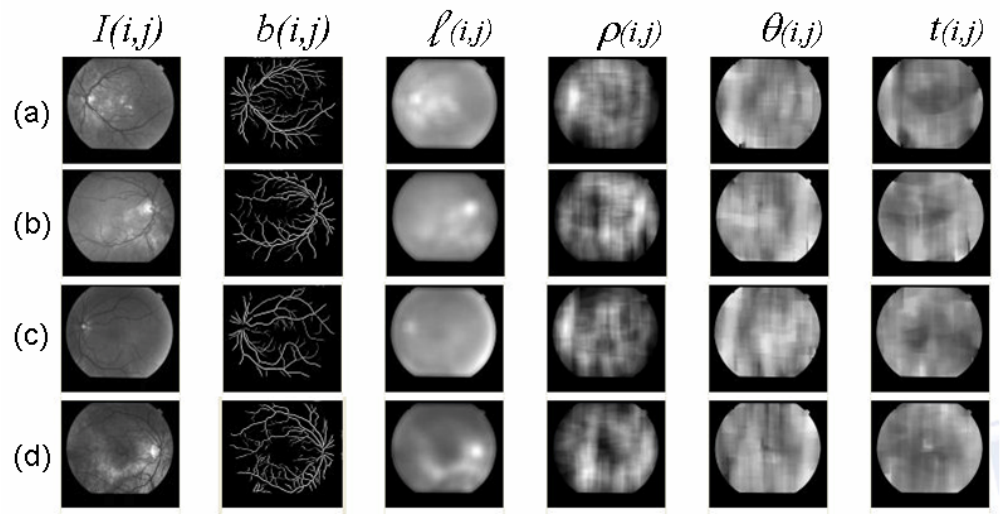

Fig. 6. Visual representations of vessel segmentation and resulting feature maps for four different fundus images in rows (a) through (d).

2.3. Classification

For classification of each image pixel as ON or not ON, we assume a multivariate normal density function [20] for the distribution of the data. A two-class Bayesian discriminant function is used to assign each location in the classification image, $\omega(i,j)$, a value of 0 or 1 according to,

$$\omega(i,j)=\begin{cases}0 & if\ \ g_0(i,j)\geq g_1(i,j)\\ 1 & if\ \ g_0(i,j)<g_1(i,j)\end{cases}\ , \qquad \textbf{Eq. 5}$$

The discriminant functions, g_0 ad g_1, are defined by,

$$g_0(i,j)=\frac{p(\omega_0)}{2\pi\sum_o}e^{-(v-\mu_o)^t\Sigma_o^{-1}(v-\mu_o)}\quad and\quad g_1(i,j)=\frac{1-p(\omega_0)}{2\pi\sum_1}e^{-(v-\mu_1)^t\Sigma_1^{-1}(v-\mu_1)}, \qquad \textbf{Eq. 6}$$

where Σ_0 and Σ_1 are the covariance matrices and μ_0 and μ_1 are the population means generated from the training features for each class. The function $p(\omega_o)$ is the probability in the training data of a position (i,j) belonging to the ON region of the image. The top row of Fig. 7 shows four examples of classification maps, $\omega(i,j)$, for the corresponding rows of data in Fig. 6. Once these maps have been obtained, the most likely ON coordinate (i_{ON},j_{ON}) is determined by applying the prior probability map, $P(i,j)$, introduced in Fig. 2 (a) as follows:

$$\begin{bmatrix} i_{ON} \\ j_{ON} \end{bmatrix} = \arg\max_{(i,j)}[\,\omega(i,j)\cdot P(i,j)\,]\ . \qquad \textbf{Eq. 7}$$

The bottom row of Fig. 7 shows corresponding estimates of the location of the ON for the classification maps shown in the top row. Note that the "correct" versus "incorrect" classification of the ON coordinate is based on a comparison to a manually selected coordinate in the test data. A "correct" location of the ON is defined for any estimated coordinate whose distance from the manually selected point is less than one ON diameter.

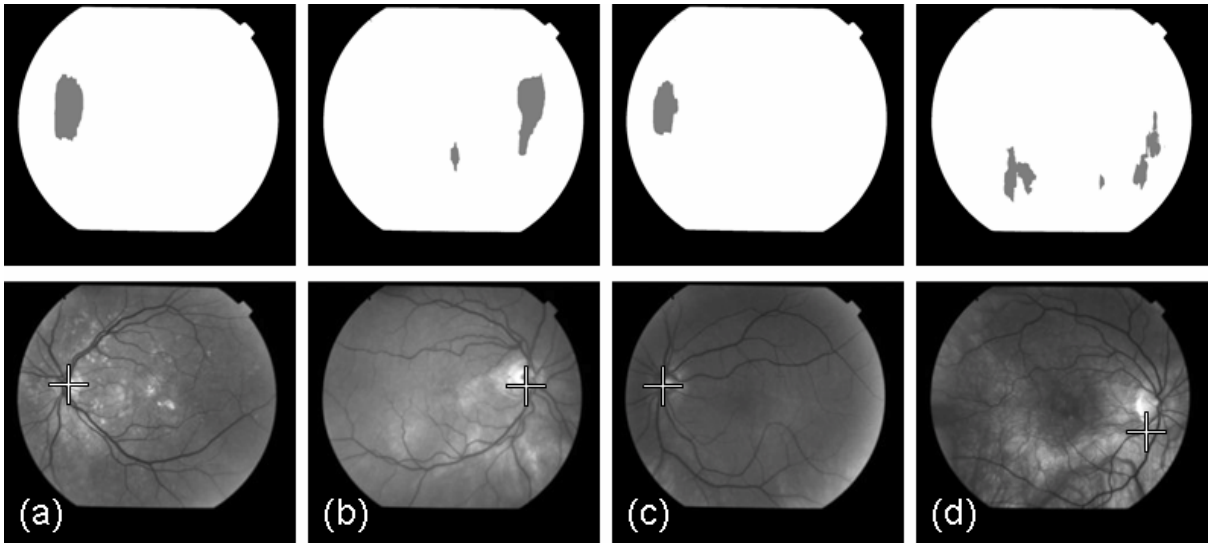

Fig. 7. Pixel classification maps (top row) and detected ON locations (bottom row) corresponding to (a)-(d) in the previous figure. Note that (a)-(c) show correct detection (i.e., within 1 diameter of the known ON location) and (d) shows an incorrect detection (within 2 diameters of the ON).

3. RESULTS

Fig. 7 represents the detection of the ON for a few examples. To characterize our method over a larger population of images, we have performed an extensive analysis on two datasets. We currently have a total population of 395 red-free fundus images representing 19 different retinal pathologies. We have performed two separate tests on this dataset. For our first test we have randomly extracted 100 images for evaluation of the efficacy of the four features defined in Section 2.2. When considering fundus images such as those shown in Fig. 6 (a)-(d), it is apparent that the brightness of the ON can be a strong indicator of the ON location. For this reason we have performed an evaluation of classifier

performance when considering only the luminance feature, ℓ, and then only the vascular features ρ, θ, and t. Finally we tested performance using all four features on this set of 100 images.

As briefly described in Section 2.3, we are defining a correct localization of the ON based on a comparison of the estimated coordinate, (i_{ON},j_{ON}), to a coordinate that was manually selected to reside at the visual center of the ON, (i_m,j_m). A coordinate was defined to be correct if the distance between the calculated and manually selected points were less than 1 ON radius (1R), which is approximately 65 pixels on average for our dataset. We also report performance for locations that are within 2R of the ON.

To perform the test on the 100 image set, we trained the Bayesian classifier using 50 images. Training consisted of determining the covariance matrices, class means, and *a-priori* probability required for the discriminant functions g_0 and g_1 defined in Eq. 6. The other 50 images were then processed to test the classifier. Next, the test data were exchanged to train the classifier and the original 50 training data were used to test. The aggregate performance across the 100 images is shown in Table 1 for the different sets of features being evaluated.

Table 1. Performance of the optic nerve detection algorithm for a set of 100 red-free fundus images exhibiting 19 different pathologies. Performance results are shown for estimates that are within one ON radius (1R) and two ON radius (2R) away from the manually selected ON coordinate. Results are shown for three different feature sets.

Pathology	No. of Examples	ℓ		ρ, θ, t		ℓ, ρ, θ, t	
		%(1R)	%(2R)	%(1R)	%(2R)	%(1R)	%(2R)
Age-related macular degeneration (AMD)	14	57.1	78.6	85.7	100.0	92.9	100.0
Cystoid macular edema (CME)	11	54.5	63.6	81.8	100.0	90.9	90.9
Choroidal neovascularization (CNV)	5	60.0	80.0	80.0	80.0	100.0	100.0
Choroidal lesion (ChL)	5	80.0	100.0	80.0	100.0	60.0	100.0
Cone dystrophy (CoDy)	1	100.0	100.0	100.0	100.0	100.0	100.0
Juxtafoveal telangiectasis (JFT)	5	40.0	40.0	100.0	100.0	80.0	100.0
Metastasis (MET)	4	50.0	50.0	100.0	100.0	100.0	100.0
Choroidal melanoma (ML)	3	100.0	100.0	66.7	100.0	66.7	100.0
Normal fundus (NM)	5	80.0	80.0	60.0	80.0	80.0	100.0
Non-proliferative diabetic retinopathy (NPDR)	19	73.7	84.2	78.9	89.5	94.7	94.7
Ocular ischemia (OIS)	2	50.0	50.0	100.0	100.0	100.0	100.0
Optic nerve lesion (ON)	3	100.0	100.0	0.0	100.0	33.3	100.0
Proliferative diabetic retinopathy (PDR)	9	77.8	100.0	100.0	100.0	88.9	100.0
Retinal artery occlusion (RAO)	4	25.0	50.0	100.0	100.0	100.0	100.0
Retinal vein occlusion (RVO)	4	25.0	50.0	100.0	100.0	100.0	100.0
Retinal detachment (ReD)	1	100.0	100.0	0.0	0.0	0.0	0.0
Retinitis pigmentosa (ReP)	1	100.0	100.0	100.0	100.0	100.0	100.0
Sickle cell disease (SC)	2	50.0	100.0	50.0	100.0	50.0	100.0
Stargardt's disease (STAR)	2	100.0	100.0	100.0	100.0	100.0	100.0
Total Performance	**100**	**65.0**	**78.0**	**82.0**	**95.0**	**87.0**	**97.0**

Note that the 1R performance improves with the inclusion of features ranging from 65% for ℓ-only to 87% for all features. This result shows that the luminance is a reasonably strong indicator of ON location as previously discussed, but that the vascular features, ρ, θ, and t, are more discriminant (as a group) and that all four features add value to the classification and ON localization process.

Our final test was performed to gain a better understanding of the performance of the method across a larger population. For this test we extracted 50 images from the original set of 395 for training and we tested on the remaining 345. The results are listed in Table 2 for both 1R and 2R performance using all four features. In summary the performance of the method on the larger set was 81% for the 1R criterion and 90% for the 2R criterion. Both the 1R and 2R performances were lower than for the 100 image set, which performed at 87% and 97% respectively. A slightly lower performance is to be expected across a larger, previously unseen image population due to the wider variation of examples in the set.

Table 2. Performance of the optic nerve detection algorithm for a set of 345 red-free fundus images exhibiting 19 different pathologies. Performance results are shown for estimates that are within one ON radius (1R) and two ON radius (2R) away from the manually selected ON coordinate. All features were used.

Pathology	No. of Examples	ℓ, ρ, θ, t	
		%(1R)	%(2R)
Age-related macular degeneration (AMD)	35	82.9	91.4
Cystoid macular edema (CME)	29	96.6	96.6
Choroidal neovascularization (CNV)	28	75.0	85.7
Choroidal lesion (ChL)	34	70.6	88.2
Cone dystrophy (CoDy)	1	100.0	100.0
Juxtafoveal telangiectasis (JFT)	13	69.2	76.9
Metastasis (MET)	4	75.0	75.0
Choroidal melanoma (ML)	29	82.8	93.1
Normal fundus (NM)	18	88.9	88.9
Non-proliferative diabetic retinopathy (NPDR)	37	94.6	94.6
Ocular ischemia (OIS)	4	75.0	100.0
Optic nerve lesion (ON)	12	66.7	91.7
Proliferative diabetic retinopathy (PDR)	34	73.5	91.2
Retinal artery occlusion (RAO)	12	75.0	100.0
Retinal vein occlusion (RVO)	28	82.1	89.3
Retinal detachment (ReD)	1	0.0	0.0
Retinitis pigmentosa (ReP)	12	83.3	91.7
Sickle cell disease (SC)	5	100.0	100.0
Stargardt's disease (STAR)	9	62.5	75.0
Total Performance	**345**	**80.8**	**90.4**

Finally, examples of four problematic images are shown in Fig. 8 below. In these examples the ON is primarily a dark feature in (a) and (b) suggesting that the luminance does not contribute to the ON identification. In (c) the retinal pigmented epithelial later is not particularly pigmented resulting in a bright background field that strongly reflects the vasculature of the choriod region below the retina. In (d) there are a large number of potentially confusing bright features associated with choroidal lesions. In all these cases the ON was reasonably located by the method described herein.

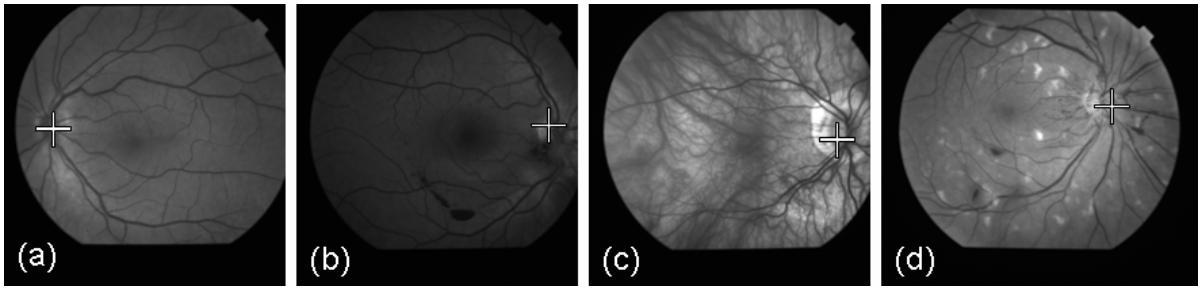

Fig. 8. Examples of correct ON detection in four fundus images of widely differing visual characteristics. In examples (a), (b), and (d) the ON is uncharacteristically dark while (c) contains confusing structure from the choroidal region below the retinal pigmented epithelial layer (due to light pigmentation). Image (d) also contains a large number of choroidal lesions.

4. CONCLUSIONS

We have presented a method for locating the optic nerve in red-free fundus imagery that takes advantage of the characteristics of the vascular structure in the retina to extract statistical features related to the vascular density, orientation, and thickness. These features are used to train and apply a Bayesian classifier that assumes a multivariate normal distribution model to classify the pixels in the original image into the binary category of optic nerve or not optic nerve. The overall performance of approximately 81%-87% correct optic nerve detection is encouraging and supports our continued research to detect other relevant structures of the retina including the macula and the variety of lesions that characterize retinal disease.

5. ACKNOWLEDGEMENTS

We would like to acknowledge The Plough Foundation, Memphis, Tennessee and Research to Prevent Blindness, New York, New York, along with the Laboratory Directed Research and Development Program of the Oak Ridge National Laboratory for their support of this research.

6. REFERENCES

[1] A.F. Amos, D.J. McCarty, P. Zimmet, "The rising global burden of diabetes and its complications: estimates and projections to the year 2010," Diabetic Med 1997;14: S57-85.
[2] Centers for Disease Control and Prevention (2003) National Diabetes Fact Sheet. (http://www.cdc.gov).
[3] C. Stellingwerf, P. Hardus, J. Hooymans, "Two-field photography can identify patients with vision-threatening diabetic retinopathy: a screening approach in the primary care setting," Diabetes Care. 2001, 24:2086-90.
[4] J.C. Javitt, L.P. Aiello, L.J. Bassi, Y.P. Chiang, J.K. Canner, "Detecting and treating retinopathy in patients with type I diabetes mellitus: Savings associated with improved implementation of current guidelines," Ophthalmology. 1991 Oct;98(10):1565-73.
[5] C. Stellingwerf, P. Hardus, J. Hooymans, "Two-field photography can identify patients with vision-threatening diabetic retinopathy: a screening approach in the primary care setting," Diabetes Care, 2001, 24:2086-90.
[6] M. Larsen, J. Godt, M. Grunkin, "Automated detection of diabetic retinopathy in a fundus photographic screening population," Invest Ophthal Vis Sci 2003, 44:767-71.
[7] D.Y. Lin, M.S. Blumenkranz, R.J. Brothers, D.M. Grosvenor, "The sensitivity and specificity of single-field nonmydriatic monochromatic digital fundus photography with remote image interpretation for diabetic retinopathy screening: a comparison with ophthalmoscopy and standardized mydriatic color photography," Am J Ophthalmol. 2002 Aug;134(2):204-13.
[8] A. Pinz, S. Bernogger, P. Datlinger, A. Kruger, "Mapping the human retina," IEEE Trans Med Imaging. 1998 Aug;17(4):606-19.
[9] P.F. Sharp, A. Manivannan, H. Xu, J.V. Forrester, "The scanning laser ophthalmoscope--a review of its role in bioscience and medicine," Phys Med Biol. 2004 Apr 7;49(7):1085-96.
[10] H. Li, O. Chutatape, "Automated feature extraction in color retinal images by a model based approach," IEEE Trans Biomed Eng. 2004 Feb;51(2):246-54.
[11] J. Morgan-Davies, N.K. Taylor, A.M. Armbrecht, P. Aspinall, B. Dhillon, "Progressive assessment of age related macular degeneration using an artificial neural network approach," Br J Ophthalmol. 2001 Feb;85(2):246-7.
[12] A.A. Cavallerano, J.D. Cavallerano, P. Katalinic, A.M. Tolson, L.P. Aiello, L.M. Aiello; Joslin Vision Network Clinical Team, "Use of Joslin Vision Network digital-video nonmydriatic retinal imaging to assess diabetic retinopathy in a clinical program," Retina. 2003 Apr;23(2):215-23.
[13] S.R. Fransen, T.C. Leonard-Martin, W.J. Feuer, P.L. Hildebrand; Inoveon Health Research Group, "Clinical evaluation of patients with diabetic retinopathy: accuracy of the Inoveon diabetic retinopathy-3DT system," Ophthalmology. 2002 Mar;109(3):595-601.
[14] M. Foracchia, E. Grisan, A. Ruggeri, "Luminosity and contrast normalization in retinal images," Medical Image Analysis, Vol.9, Issue 3, June 2005, p. 179-190.
[15] M.E. Martin-Perez, A.D. Hughes, A.V. Staanton, S.A. Thom, A.A. Bharath, K.H. Parker, "Segmentation of retinal blood vessels based on the second directional derivative and region growing," IEEE International Conference on Image Processing, 1999, Vol. 2, p. 173-176.
[16] T. Lin, Y. Zheng, "Adaptive image enhancement for retinal blood vessel segmentation," Electronic Letters, Vol. 38, Issue 19, Sep. 2002, p. 1090-1091.
[17] Z. H. Qing, "Segmentation of blood vessels in retinal images using 2-D entropies of gray level-gradient co-occurrence matrix," IEEE International Conference on Acoustics, Speech, and Signal Processing, 2004, p. 509-512.
[18] M. Foracchia, E. Grisan, A. Ruggeri, "Detection of the optic disc in retinal images by means of a geometrical model of vessel structure," IEEE Trans. on Medical Imaging, Vol. 23, No. 10, Oct. 2004, p. 1189-1195.
[19] A. Hoover, M. Goldbaum, "Locating the optic nerve in a retinal image using the fuzzy convergence of the blood vessels," IEEE Tran. on Medical Imaging, Vol. 22, No. 8, Aug. 2003, p. 951-958.
[20] R.O. Duda, P.E. Hart, D.G. Stork, Pattern Classification, 2nd Ed., John Wiley and Sons, Inc, New York, 2001.
[21] D.T. Morris, C. Donnison, "Identifying the neuroretinal rim boundary using dynamic contours," Image and Vision Computing, Vol. 17, 1999, p. 169-174.
[22] A. Hoover, M. Goldbaum, "Locating the Optic Nerve in a Retinal Image Using the Fuzzy Convergence of Blood Vessels," IEEE Trans. On Medical Imaging, Vol. 22, No. 8, 2003, p. 951-958.
[23] F. Zana, J. Klein, "Segmentation of Vessel-Like Patterns Using Mathematical Morphology and Curvature Evaluation," IEEE Trans. On Image Processing, Vol. 10, No. 7, July 2001, p. 1010-1019.
[24] W.T. Freeman, E.H. Adelson, "The Design and Use of Steerable Filters," IEEE Trans. on Pattern Analysis and Machine Intelligence, Vol. 13, No. 9, Sept. 1991, p. 891-906.